Monthly Notices
of the
ROYAL ASTRONOMICAL SOCIETY

MNRAS **511,** 3487–3500 (2022)
Advance Access publication 2022 February 2

https://doi.org/10.1093/mnras/stac293

Young Exoplanet Transit Initiative follow-up observations of the T Tauri star CVSO 30 with transit-like dips

R. Bischoff,[1]★ St. Raetz,[2] M. Fernández,[3] M. Mugrauer,[1] R. Neuhäuser,[1] P. C. Huang,[4] W. P. Chen,[4,5] A. Sota,[3] J. Jiménez Ortega,[3] V. V. Hambaryan,[1,6] P. Zieliński,[7,8] M. Dróżdż,[9] W. Ogłoza,[9] W. Stenglein,[1] E. Hohmann[1] and K.-U. Michel[1]

[1]*Astrophysical Institute and University Observatory, Friedrich-Schiller-Universität Jena, Schillergäßchen 2, D-07745 Jena, Germany*
[2]*Institute for Astronomy and Astrophysics Tübingen, Eberhard-Karls-Universität Tübingen, Sand 1, D-72076 Tübingen, Germany*
[3]*Instituto de Astrofísica de Andalucía, CSIC, Apartado 3004, E-18080 Granada, Spain*
[4]*Graduate Institute of Astronomy, National Central University, 300 Zhongda Road, Zhongli, Taoyuan 32001, Taiwan*
[5]*Department of Physics, National Central University, 300 Zhongda Road, Zhongli, Taoyuan 32001, Taiwan*
[6]*Byurakan Astrophysical Observatory, Byurakan 0213, Aragatzotn, Armenia*
[7]*Institute of Astronomy, Faculty of Physics, Astronomy and Informatics, Nicolaus Copernicus University in Toruń, ul. Grudziądzka 5, PL-87-100 Toruń, Poland*
[8]*Astronomical Observatory, University of Warsaw, Al. Ujazdowskie 4, PL-00-478 Warszawa, Poland*
[9]*Mt. Suhora Observatory, Pedagogical University, ul. Podchorazych 2, PL-30-084 Krakow, Poland*

Accepted 2022 January 27. Received 2022 January 13; in original form 2021 November 12

ABSTRACT

The T Tauri star CVSO 30, also known as PTFO 8-8695, was studied intensively with ground-based telescopes as well as with satellites over the last decade. It showed a variable light curve with additional repeating planetary transit-like dips every ∼10.8 h. However, these dimming events changed in depth and duration since their discovery and from autumn 2018 on, they were not even present or near the predicted observing times. As reason for the detected dips and their changes within the complex light curve, e.g. a disintegrating planet, a circumstellar dust clump, stellar spots, possible multiplicity, and orbiting clouds at a Keplerian co-rotating radius were discussed and are still under debate. In this paper, we present additional optical monitoring of CVSO 30 with the meter class telescopes of the Young Exoplanet Transit Initiative in Asia and Europe over the last 7 yr and characterize CVSO 30 with the new Early Data Release 3 of the European Space Agency-*Gaia* mission. As a result, we describe the evolution of the dimming events in the optical wavelength range since 2014 and present explanatory approaches for the observed variabilities. We conclude that orbiting clouds of gas at a Keplerian co-rotating radius are the most promising scenario to explain most changes in CVSO 30's light curve.

Key words: stars: individual: CVSO 30 – stars: variables: T Tauri – techniques: photometric.

1 INTRODUCTION

While most exoplanets are Gyr old, including in particular transiting planets, it would be best to study planet formation and early evolution with young planets (age <100 Myr). Therefore, the Young Exoplanet Transit Initiative (YETI; Neuhäuser et al. 2011) searched for planet candidates in young open stellar clusters. One of our first targets was the 25 Ori cluster, which was observed within the YETI network since 2010. As a result, we could confirm the detection of a transit-like signal within the light curve of CVSO 30, which was first found by van Eyken et al. (2012). Schmidt et al. (2016) discovered an additional wide companion planet candidate via direct imaging. CVSO 30, which is also known as PTFO 8-8695, is a weak-line T Tauri star with spectral type M3 (Briceño et al. 2005), which showed initially brightness dips of ∼35 mmag every ∼10.8 h lasting about 100 min. However, shape, depth, and duration of these dips changed significantly over time as reported by van Eyken et al. (2012) and Raetz et al. (2016). Furthermore, the dimming events can show either no wavelength dependence (Raetz et al. 2016) or, in other epochs, depths that decrease at larger wavelengths (Yu et al. 2015; Onitsuka et al. 2017; Tanimoto et al. 2020). On the one hand, CVSO 30 seems to show no dimming at some epochs (Koen 2015) and on the other hand, multiple dips per period were detected. Tanimoto et al. (2020) monitored CVSO 30 intensively in the *I*- band and in JHK_s- filters between 2014 and 2018. They found that CVSO 30 showed three different fading events, namely, 'dip-A', 'dip-B', and 'dip-C'. The dip-A appeared 0.1 earlier in phase compared to the dimming reported in van Eyken et al. (2012), which they called 'dip-B'. Another 'dip-C' was discovered in November 2018, 0.5 later in phase. As diverse as the detected changes in CVSO 30's light curve were also the attempts to explain their origin during the last decade. van Eyken et al. (2012) argued that the signal was caused by a Jovian planet based on radial velocity (RV) measurements and adaptive optics imaging, where no significant RV variation or background source could be detected. In order to explain the changing depth, duration as well as the disappearance and reappearance of the transit-like signal, Barnes et al. (2013) proposed a misalignment between the rotational axis of the star and the orbital plane of a precessing planet. This hypothesis agrees with Ciardi et al. (2015), but the model

★ E-mail: richard.bischoff@uni-jena.de

Table 1. Observatories and instruments of the YETI network, which took part in the follow-up observations.

Observatory	Abbrev.	Long. (E) (deg)	Lat. (N) (deg)	Altitude (m)	Mirror ⌀ (m)	CCD	# Pixel	field of view (FoV) (arcmin)
Lulin/Taiwan	LOT	120.5	23.3	2862	1.0	Apogee U42[a]	2048 x 2048	11.0 x 11.0
Suhora/Poland	Suhora	20.1	49.6	1009	0.6	Apogee Aspen CG47[b]	1024 x 1024	20.0 x 20.0
Jena/Germany	GSH	11.5	50.9	367	0.9[c]	E2V CCD42-40[d]	2048 x 2048	52.8 x 52.8
Tübingen/Germany	IAAT	9.1	48.5	400	0.8	SBIG ST-L-1001E[e]	1024 x 1024	13.6 x 13.6
Sierra Nevada/Spain	OSN	− 3.4	37.1	2896	1.5	VersArray:2048B[f]	2048 x 2048	7.9 x 7.9
Tenerife/Spain	OGS	− 16.5	28.3	2393	1.0	EEV 42-40[g]	4 x [2048 x 2048]	42.5 x 42.5

Notes. [a]Huang et al. (2019). [b]Siwak et al. (2019). [c]0.6 m in Schmidt mode. [d]Mugrauer & Berthold (2010).
[e]http://astro.uni-tuebingen.de/about/teleskop/telkam.shtml . [f]Ortiz et al. (2006).
[g]http://research.iac.es/OOCC/iac-managed-telescopes/ogs/.

needed further fine tuning to fit their photometric and spectroscopic data. In contrast to this, the planetary scenario is considered unlikely by Yu et al. (2015), because the target does not show the Rossiter–McLaughlin effect (RME) or changes in its RV between 2011 and 2013. Also star spots are usually visible for half a rotational period and this contradicts the short duration of the observed fading events. Even if multiple stellar spots were considered, this scenario could reproduce the signal, but it is based on assuming a complex, and stable pattern (Yu et al. 2015). Tanimoto et al. (2020) suggest the idea that the original fading event in van Eyken et al. (2012) consists of a periodically combined dust cloud and a precessing planet, which split up in 2014 to explain the detection of multiple dips per period near the predicted observing times. Additionally, the newly found dip-C could be the result of an accretion hotspot or a dust cloud. Recent publications of Bouma et al. (2020) and Koen (2020) showed that the light curve from the Transiting Exoplanet Survey Satellite (*TESS*; Ricker et al. 2015) contains two different periods (11.98 and 10.76 h) and that CVSO 30 can be a binary star with no planetary companion. Bouma et al. (2020) presented also several other possible explanations, which need to be considered further. Koen (2021) combined the binary scenario with star-spot models to explain the variability of CVSO 30 based on *TESS* measurements in one passband. However, a filling factor of roughly 0.5 seems by far too large for normal spots and would have been probably detected in previous high-resolution, high signal-to-noise spectra, as e.g. in the case of the weak-line T Tauri star P1724 in Neuhauser et al. (1997).

In this paper, we describe our observations in the optical wavelength range in Section 2. In Section 3, we explain the data reduction and the routine for photometric measurements. The following Section 4 presents our light-curve analysis. We test scenarios for the cause of CVSO 30's variability in Section 5. Our results are discussed and we give a conclusion in the final section of this paper.

2 OBSERVATIONS

In contrast to the original YETI campaigns, where the 25 Ori cluster was continuously monitored for 7–12 subsequent nights within multiple runs in several years, we focused this time completely on the predicted time slots of the dimming event, according to ephemeris presented in Raetz et al. (2016). An overview of the involved observatories and instrumentation, which participated within our YETI follow-up observations of CVSO 30 since autumn 2014, is given in Table 1. Each monitoring includes typically about 1 h of observation time before and after the start/end of the predicted dimming event. The observations were usually carried out in the *R*-band filter with individual image integration times up to a few minutes, as listed in the observation log in Table 2, for sufficient

Table 2. Observation log. Summary of all follow-up observations of CVSO 30 within the YETI network since 2014. For each epoch, we list the associated observing date (start of observations), site, used filter, number of exposures (N_{exp}), and individual detector integration time (DIT) of each frame.

Date	Observatory	Filter	N_{exp}	DIT (s)
2014 Oct 23	OSN	R	172	90
2014 Oct 28	OSN	R	165	90
2014 Nov 2	GSH	R	66	180
2014 Nov 6	OSN	R	145	100
2014 Nov 19	OSN	R	62	90
2014 Dec 11	OSN	R	125	100
2015 Feb 11	GSH	R	74	180
2015 Nov 14	OGS	R	60	210
2015 Nov 19	OGS	Clear	103	135
2015 Nov 23	OSN	R	76	180
2016 Feb 2	OSN	R	100	180
2016 Oct 26	OSN	R	30	180
2017 Jan 5	OSN	R	69	240
2017 Jan 14	OSN	R	13	240
2017 Jan 23	OSN	R	86	180
2017 Oct 27	OSN	R	70	200
2017 Nov 13	OSN	R	84	200
2017 Nov 22	OSN	R	67	200
2017 Nov 22	GSH	R	106	120
2018 Jan 23	OSN	R	123	200
2018 Feb 14	IAAT	Clear	124	120
2018 Oct 14	GSH	R	47	210
2018 Oct 31	Suhora	V, I	80, 80	120, 60
2018 Nov 8	LOT	R	60	120
2018 Nov 9	GSH	R	32	300
2018 Nov 14	GSH	R	50	210
2018 Dec 1	OSN	R	85	180
2018 Dec 4	LOT	R	136	120
2018 Dec 9	LOT	R	47	120
2018 Dec 13	LOT	R	80	120
2018 Dec 17	LOT	R	137	120
2018 Dec 18	LOT	R	137	120
2018 Dec 26	LOT	R	37	120
2018 Dec 27	LOT	R	137	120
2019 Oct 31	GSH	R	65	180
2019 Nov 9	GSH	R	52	180
2019 Dec 5	GSH	R	78	180
2020 Jan 15	GSH	R	53	180
2020 Jan 23	GSH	R	60	180
2020 Feb 7	GSH	R	38	180
2020 Oct 20	GSH	R	62	180
2020 Nov 23	GSH	R	77	180
2020 Nov 25	GSH	R	63	180
2021 Jan 11	OSN	R	66	200
2021 Jan 15	OSN	R	79	200
2021 Jan 29	OSN	R	139	90
2021 Feb 2	OSN	R	82	200

photometric precision and time resolution.

After receiving message from T. O. B. Schmidt (private communication) in summer 2019, who reported a phase shifted dimming within the *TESS* light curve of CVSO 30, we extended our monitoring also to these additional time slots. Tanimoto et al. (2020) had found this signal independently within their data in November 2018.

Our photometric follow-up observations of CVSO 30 have a total integration time of about 164.4 h spanning over the range of time between 2014 October and 2021 February.

3 DATA REDUCTION AND PHOTOMETRY

The data were processed with standard image-reduction routines based on IRAF[1] (Tody 1993), which include bias, dark, and flat-field correction.

With our routine, we can perform photometry on all stars within the field of view simultaneously. Therefore, we create a list of pixel coordinates for all detectable light sources with SOURCE EXTRACTOR (SExtractor; Bertin & Arnouts 1996). This list was then used as a reference to remove tracking offsets between the individual images, which was also carried out with SExtractor. We determined the optimal aperture size with IRAF for each night separately, by using 15 different apertures, ranging from one up to two average full width at half-maximum (FWHM) of point sources, detected in the individual observing nights. The standard deviations of the instrumental magnitude differences, of a subset of the brightest, non-variable stars, were then calculated for all 15 apertures, and we chose as optimal aperture the one, with the smallest sum of standard deviations. The optimized aperture was then utilized for aperture photometry on all stars within the field of view.

At next, we performed differential photometry with the program PHOTOMETRY from Broeg, Fernández & Neuhäuser (2005), which creates an artificial comparison star. This artificial star includes information of all detected stars, but they are weighted depending on their stability during the observation. Variable stars have typically a higher standard deviations during the processed time series and therefore, they are weighted lower than stable stars. For more details on the used photometry routine, see Errmann et al. (2014) or Errmann (2016).

Finally, we get a list for each star within the field of view, which includes the heliocentric Julian date (HJD), the determined relative magnitude, and its uncertainty.

4 LIGHT CURVE ANALYSIS

The unprocessed light curves are shown in Appendix A. Since CVSO 30 is a T Tauri star, its light curve is impacted by stellar variability which had to be considered and characterized before further investigation. We treated every light curve individually and detrended them by fitting polynomials of the third order to the out-of-event measurements. This was done for the listed nights in Table A1, which exhibit sufficient out-of-event observing time. The nights without significant fading events were not included in Table A1, but they are presented in Figs A1–A7. The detrended (if applicable) and also the original photometric measurements of all light curves are provided as online supplementary material.

[1]IRAF is distributed by the National Optical Astronomy Observatories, which are operated by the Association of Universities for Research and Astronomy, Inc., under cooperative agreement with the National Science Foundation.

Table 3. Properties of the detected flare-like events during our monitoring campaign.

Date	Observatory	Maximal flux increase (per cent)
2018 Jan 23	OSN	10.1 ± 0.8
2018 Nov 14	GSH	4.7 ± 1.0
2018 Dec 27	LOT	3.5 ± 0.5

Table 4. Physical parameters of the CVSO 30.

Parameter	Value	Ref.
RA (J2000; h : m : s)	05 : 25 : 07.6	1
Dec (J2000; deg : m : s)	+01 : 34 : 24.5	1
Mass M ($M_\odot$)	0.502 ± 0.038	2
Radius R ($R_\odot$)	1.69 ± 0.16	This work
Effective temperature $T_{\rm eff}$ (K)	$3448\ ^{+43}_{-12}$	2
Surface gravity log (g) (dex)	$3.84\ ^{+0.02}_{-0.04}$	2
Metallicity [Fe/H] (dex)	0.500 ± 0.001	2
Distance d (pc)	$334\ ^{+4}_{-3}$	3
Age (Myr)	8.5 ± 1.2	4
Apparent brightness $m_{\rm G}$ (mag)	15.101 ± 0.003	5
Extinction $A_{\rm G}$ (mag)	0.195 ± 0.049	This work
Absolute brightness $M_{\rm G}$ (mag)	$7.286\ ^{+0.075}_{-0.078}$	This work

Note. 1: Briceño et al. (2005); 2: Queiroz et al. (2020); 3: Bailer-Jones et al. (2021); 4: Kounkel et al. (2018); 5: Gaia Collaboration (2021).

Furthermore, we found within our light curves three flare-like events. Their flux increase was determined by fitting third order polynomials to the unprocessed photometric measurements outside the flare-like event and then comparing the expected flux, given by the polynomial, to the corresponding actual measurement during the flare. The associated results are given in Table 3.

4.1 Transit fitting

The detrended light curves of CVSO 30 were further analysed using the 'Exoplanet Transit Database' (ETD; Brát et al. 2010; Poddaný, Brát & Pejcha 2010).

ETD is an on-line portal, which can be utilized to fit synthetic transit light curves to observational data. The website determines mid-time, duration, and depth of the fading event by using non-linear least-squares algorithm and also removing systematic trends by a second-order polynomial (Brát et al. 2010). As input parameter, a first estimation of the mid-transit time and transit duration are needed together with the radii ratio of host star and companion, as well as the impact parameter and the linear limb-darkening coefficient. These variables were obtained from stellar mass, radius, and orbital period, as listed in Table 4. The linear limb-darkening coefficient for the R-band filter ($u = 0.717 \pm 0.033$) is estimated, based on the given effective temperature and surface gravity, from the work of Claret & Bloemen (2011).

The radius of CVSO 30 was determined by calculating its bolometric magnitude

$$M_{\rm bol} = M_{\rm G} + BC_{\rm G}, \quad (1)$$

where $M_{\rm G}$ is the absolute brightness in the G-band (see Section 5.2 for details) and $BC_{\rm G}$ the corresponding bolometric correction. We derived $BC_G = (-1.445 \pm 0.072)$ mag from the website of 'MESA Isochrones & Stellar Tracks',[2] (Choi et al. 2016), taking into account

[2]http://waps.cfa.harvard.edu/MIST/model_grids.html

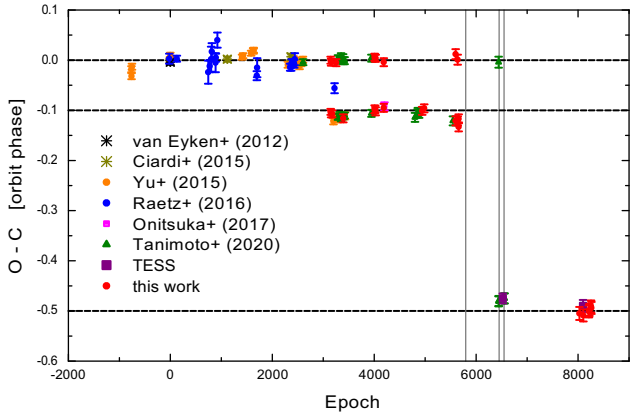

Figure 1. The O–C diagram of CVSO 30. Only complete fading events from Raetz et al. (2016) are plotted. The epochs with detected flare-like events are illustrated as grey vertical lines.

CVSO 30's effective temperature, extinction, metallicity, and surface gravity (values in Table 4). At next, we used

$$M_{\rm bol} = M_{\rm bol,\odot} - 2.5 \log \left(\frac{L}{\rm L_\odot} \right) \tag{2}$$

to calculate CVSO 30's luminosity (using $M_{\rm bol,\odot} = 4.74$ mag from Prša et al. 2016) and via

$$R \approx \left(\frac{L}{\rm L_\odot} \right)^{0.5} \cdot \left(\frac{T_{\rm eff,\odot}}{T_{\rm eff}} \right)^2 \cdot \rm R_\odot \tag{3}$$

its radius. The optimal light curve parameters are found with ETD by iterating the input parameter until the output parameters are consistent with each other, within their one sigma uncertainties, in five consecutive fitting attempts. ETD needs as input parameters the limb-darkening, the impact factor, the radii ratio of the planet candidate and the star, as well as a specification of the expected transit centre time and duration. The best-fitting parameters for all detected dimming events are listed in Table A1. We use the designation of Tanimoto et al. (2020) to distinguish the three phase-shifted fading events of CVSO 30. The transit centre times of the detected dimming events were converted from $\rm HJD_{UTC}$ into $\rm BJD_{TDB}$ with the online converter,[3] based on Eastman, Siverd & Gaudi (2010).

4.2 Investigation of the three phase-shifted dimming events

We found three different dimming events within our observations, which we call dip-A, dip-B, and dip-C based on the work of Tanimoto et al. (2020). Furthermore, their ephemeris

$$\begin{aligned} T_0[\rm BJD_{TDB}] &= 2455543.943 \pm 0.002, \\ P[\rm d] &= 0.4483993 \pm 0.0000006, \end{aligned} \tag{4}$$

work excellent to predict the occurrence of dip-B within our data, as shown in Appendix A and also to characterize the temporal occurrence of dip-A and dip-C. We show the 'observed minus calculated' (O–C) diagram in Fig. 1 for our detected fading events together with data from van Eyken et al. (2012), Ciardi et al. (2015), Yu et al. (2015), Raetz et al. (2016), Onitsuka et al. (2017), Tanimoto et al. (2020), and *TESS*, spanning over a decade of observations. Each dip considered separately shows no significant phase shift within its $3\,\sigma$ uncertainties. Therefore, further updates on their ephemeris are not necessary. The detrended and phase-folded light curves with the best-fitting models are shown in Figs 2 and 3.

As expected, dip-B occurs on average at phase 0.002 ± 0.005 for our observations, using its ephemeris, given in equation (4). Dip-A was visible at an average orbit phase of -0.108 ± 0.012 and dip-C at -0.500 ± 0.007 during our monitoring campaign, in comparison to dip-B. We have found flare-like events within CVSO 30's light curve and their temporal appearances are indicated as grey vertical lines in Fig. 1. The strongest flare-like event took place after the last significant detection of dip-A and dip-B, and before the first appearance of dip-C. The chronological development of the depths and durations for the three different dimming events are shown in Fig. 4. The average depth of dip-A $\Delta m_{\rm A} = (19.4 \pm 4.5)$ mmag indicates that dip-A has a comparable depth to dip-B with $\Delta m_{\rm B} = (13.1 \pm 6.6)$ mmag over the whole monitoring campaign. However, dip-B seems to be significantly deeper in season 2015/2016 with $\Delta m_{\rm B15/16} = (19.4 \pm 4.6)$ mmag in comparison to the detections in all other seasons $\Delta m_{\rm B\ other} = (8.1 \pm 0.8)$ mmag. Both, dip-A and dip-B, were not observable anymore since autumn 2017, as illustrated in Figs A5–A7. This contradicts the report in Tanimoto et al. (2020), namely that they have detected dip-B on 2018 November 9. This mentioned detection is also consistent with noise. Dip-C has an average depth of $\Delta m_{\rm C} = (30.3 \pm 6.9)$ mmag.

During our follow-up observations dip-A shows an average duration of $T_{14\,\rm A} = (66.6 \pm 21.5)$ min, while dip-B and dip-C last on average $T_{14\,\rm B} = (60.2 \pm 24.8)$ min and $T_{14\,\rm C} = (127.3 \pm 19.6)$ min.

5 EXPLANATORY APPROACHES FOR THE OBSERVED VARIABILITIES

5.1 Comparison with Tanimoto et al. (2020)

In this subsection, we are following the explanation approaches of Tanimoto et al. (2020), who give four possible explanations for the dimming events, namely (i) a cool star-spot, (ii) an accretion hotspot, (iii) a Jovian planet, and (iv) a circumstellar dust clump and test them in the context of their photometric measurements in the near-infrared. We will investigate all these scenarios for the individual dimming events, which were not ruled out already by Tanimoto et al. (2020), based on our observations.

A circumstellar dust clump, consisting of an opaque core and an optically thin dust halo, was the only remaining cause for dip-A which was not falsified. The observed fading of the flux $\delta_{\rm obs}(\lambda)$ at a particular wavelength is described by

$$\delta_{\rm obs}(\lambda) = f_{\rm core} + f_{\rm halo}\tau_{\rm V} \left[a(\lambda^{-1}) + \frac{b(\lambda^{-1})}{R_{\rm V}} \right], \tag{5}$$

with the filling factor of the core $f_{\rm core}$ and the dust halo $f_{\rm halo}$. The depth in the *V*- band is given by $\tau_{\rm V}$, and $a(\lambda^{-1})$ and $b(\lambda^{-1})$ are wavelength-dependent coefficients, as defined by Cardelli, Clayton & Mathis (1989). The ratio

$$R_{\rm V} = \frac{A_{\rm V}}{E(B-V)},$$

was determined by Tanimoto et al. (2020) to be $R_{\rm V} = 5.3$ for dip-A in both, season 2014 and 2016, based on its wavelength dependence. The corresponding best-fitting values for season 2014 are $f_{\rm core} = 0.01$, $f_{\rm halo}\tau_{\rm V} = 0.014$ and for season 2016 $f_{\rm core} = 0.005$, $f_{\rm halo}\tau_{\rm V} = 0.0135$. Given these constraints from Tanimoto et al. (2020), we found that the typical *R*-band depths of dip-A for the corresponding seasons, namely $\delta_{\rm dip\text{-}A} = 0.020 \pm 0.005$ and $\delta_{\rm dip\text{-}A} = 0.016 \pm 0.009$, from

[3] https://astroutils.astronomy.osu.edu/time/hjd2bjd.html

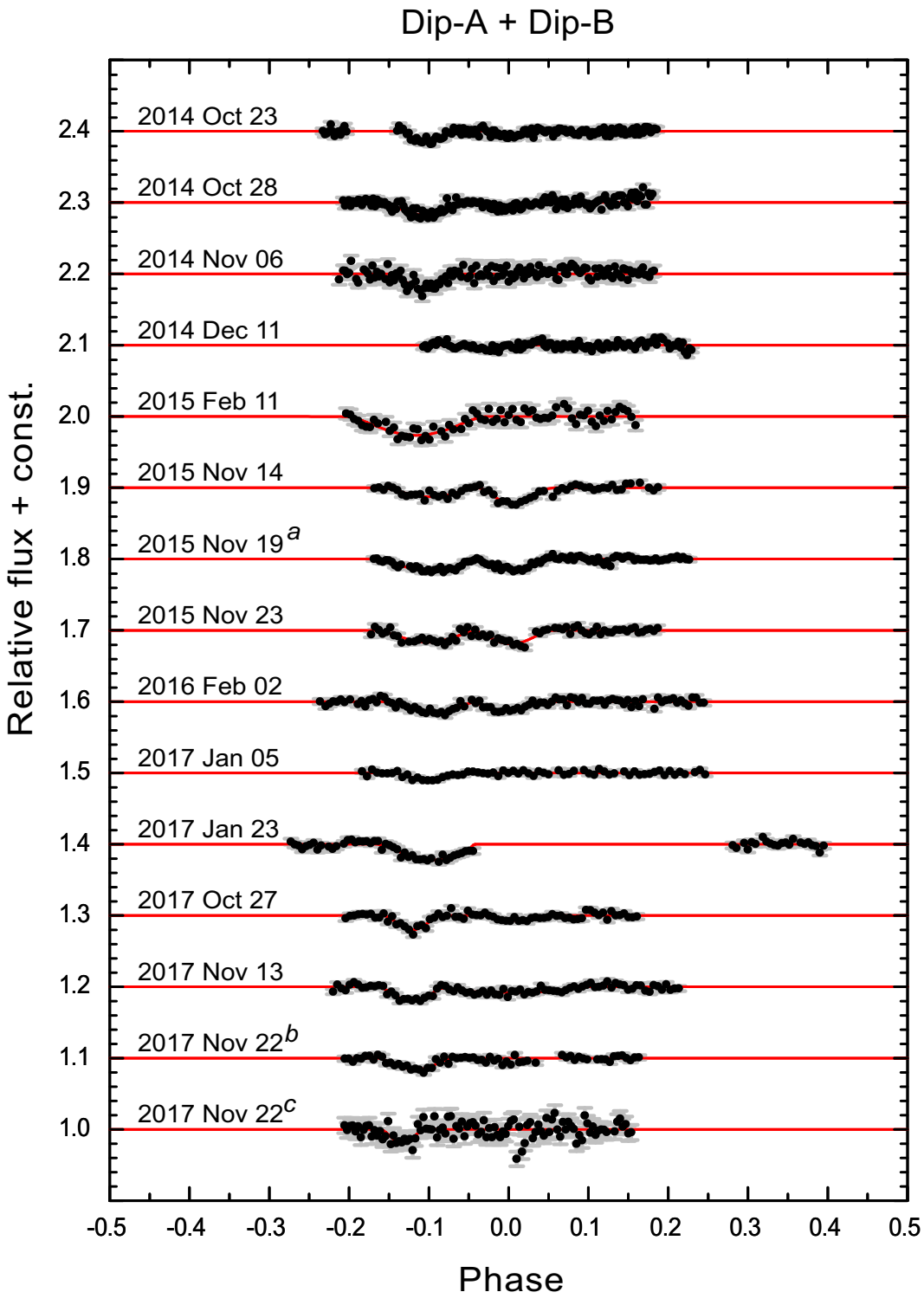

Figure 2. Detrended and phase-folded *R*-band light curves of dip-A and dip-B according to the ephemeris in equation (4). [a] clear filter, [b] OSN, and [c] GSH.

our measurements fulfil equation (5) within their $1\,\sigma$ uncertainties. Hence, we cannot rule out this scenario for dip-A.

A precessing Jovian planet and a dust clump were the remaining explanations for dip-B. However, the planet hypothesis faces some difficulties, namely the proposed changing inclination with a period of ∼1411 d is based on the proclaimed detection of dip-B on 2018 November 9, which we cannot confirm with our observations of season 2018/2019 in Fig. A5. We stress that the presumable planet was never confirmed by RV detections, but a planet scenario was just consistent with RV non-detections. Furthermore, dip-B seems to be in 2015/2016 typically twice as deep in comparison to other seasons from our follow-up observations. This feature makes a precessing planet even more questionable. Testing the dust-clump hypothesis with the derived $R_V = 5.3$, $f_{core} = 0.003$, and $f_{halo}\tau_V = 0.0027$ from

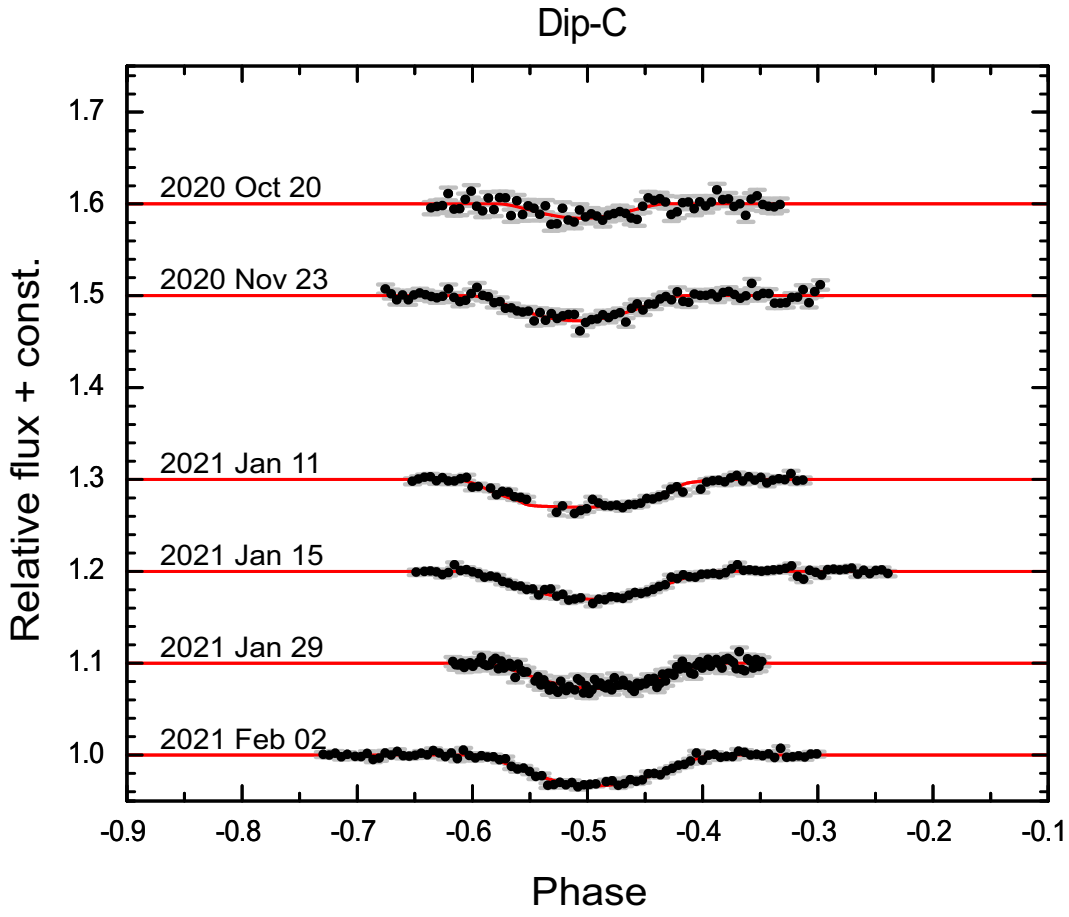

Figure 3. Detrended and phase-folded *R*-band light curves of dip-C according to the ephemeris in equation (4).

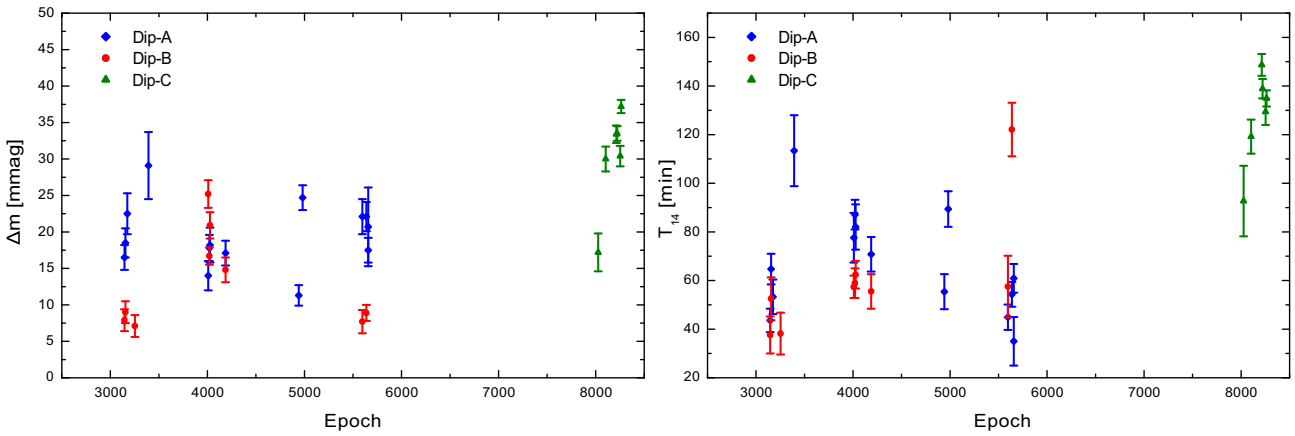

Figure 4. Chronological development of the depths (left-hand panel) and durations (right-hand panel) for the phase-shifted fading events of CVSO 30 as measured within our follow-up observations in the *R*-band.

Tanimoto et al. (2020), shows that these values fit with our observed depths of $\delta_{\text{dip-B}} = 0.007 \pm 0.001$ and $\delta_{\text{dip-B}} 0.008 \pm 0.001$ for season 2014/2015 and 2017/2018, respectively within $2\,\sigma$. However, they are slightly outside the $3\,\sigma$ interval for the average depth $\delta_{\text{dip-B}} = 0.018 \pm 0.004$ in season 2015/2016 in the *R* band.

Dip-C is considered to be either an accretion hotspot or also a circumstellar dust clump. The rotational axis of the star has to be inclined for the hotspot scenario, so that the accreting hotspot, which is brighter than the typical surface area of CVSO 30, is not visible for the observer during the fading event. The flux depth of a fading event at any wavelength, can therefore be described as

$$\delta_{\text{hot}}(\lambda) = \frac{f[B_\lambda(T_{\text{hot}}) - B_\lambda(T_\star)]}{(1-f)B_\lambda(T_\star) + f\,B_\lambda(T_{\text{hot}})}, \tag{6}$$

where f is the filling factor and T_{hot} the temperature of the hotspot (Tanimoto et al. 2020). $T_\star$ represents the effective temperature of the

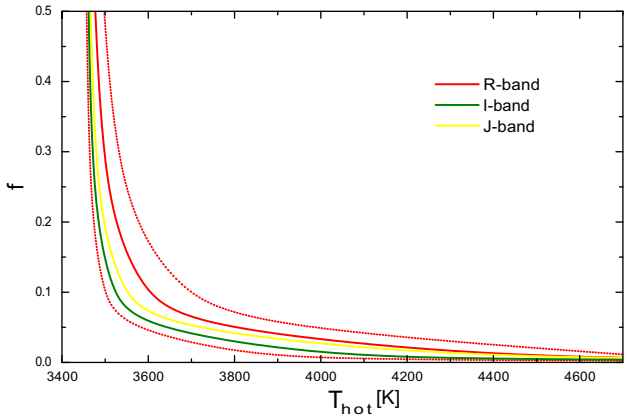

Figure 5. Contour map for dip-C's recorded depths of the dimming events. We show the possible combinations of filling factor f and temperature $T_{\rm hot}$ for an accretion hotspot in different filters. The red dotted lines are the borders of the $3\,\sigma$ intervals for the R-band.

star and B_λ is the brightness for blackbody radiation at a particular wavelength. We use the variables f and $T_{\rm hot}$ to create the contour map for our observed dimming events of dip-C and those given in Tanimoto et al. (2020). The average depths in all filters are consistent with each other within $3\,\sigma$ uncertainties as illustrated in Fig. 5. On the other hand, the average depth of $\delta_{\rm dip\text{-}C} = 0.028 \pm 0.006$ in the R-band also satisfies the values $R_{\rm V} = 5.3$, $f_{\rm core} = 0.0065$, and $f_{\rm halo}\tau_{\rm V} = 0.009$ for a possible circumstellar dust clump within $3\,\sigma$. Hence, we can neither exclude the hotspot nor the dust clump scenario for dip-C based on the R-band photometry.

We have additionally checked if dip-C was detected before 2018 and could be a secondary eclipse of dip-B. The light curves in Raetz et al. (2016) sufficiently cover multiple times the phase of ∼0.5 between 2011 and 2013. During this span of time no fading event of dip-C was detected and therefore, we can exclude this hypothesis.

5.2 Comparison with cluster members

We used the recently published data from the Early Data Release 3 of the European Space Agency (ESA)-*Gaia* mission (*Gaia* EDR3; Gaia Collaboration 2021) to identify members of the 25 Ori cluster and compare them to CVSO 30. Therefore, we searched around its prominent member, namely the star 25 Ori, within a radius of 61 arcmin for cluster members based on parallax (π) and proper motion (μ). This search radius takes into account the assumption, that stellar clusters have typical radii up to 5 pc (Unsöld & Baschek 2005), which corresponds to ∼51 arcmin based on the parallax value of 2.9321 mas for the star 25 Ori in *Gaia* EDR3. We added further 10 arcmin to this radius, in order not to miss a potential cluster member.

Thereby only sources with significant detected parallaxes and proper motions ($\frac{\pi}{\sigma(\pi)} \geq 3$, $\frac{\mu}{\sigma(\mu)} \geq 3$) were taken into account. The cluster shows an accumulation at $\pi \sim 2.9$ mas within the cumulative distribution function and a common proper motion of $\mu_{\rm RA} \sim 1.4$ mas yr^{-1} in right ascension, but no significant movement towards declination $\mu_{\rm Dec} \sim 0$ mas yr^{-1}. We used at next only stars within sufficiently large intervals around these measurements and performed sigma clipping to identify the most probable cluster members. In total, 239 objects were identified which exhibit on average $\pi = (2.8775 \pm 0.0718)$ mas and $\mu_{\rm RA} = (1.414 \pm 0.241)$ mas yr^{-1}, while no significant proper motion in declination ($\mu_{\rm Dec} = -0.256 \pm 0.580$ mas yr^{-1}) is detectable.

Based on the photometry of *Gaia* EDR3, together with distances from Bailer-Jones et al. (2021) and interstellar extinction from the dust maps of Green et al. (2019), we create the colour–magnitude diagram (CMD) of the 25 Ori cluster as illustrated in Fig. 6. The extinction values were converted into the required passbands using the relations of Wang & Chen (2019).

Here, we can confirm the results of Koen (2020) and Bouma et al. (2020) that CVSO 30 is about 0.75 mag brighter than the typical cluster member with comparable colour. This is an indication that CVSO 30 can be a binary consisting of stellar components with comparable brightness. In this case, we have to modify $M_{\rm G}$ from Table 4 into $\tilde{M}_{\rm G} = 8.039^{+0.075}_{-0.078}$ mag for a single star and following the above procedure, the resulting radius of one stellar component is $\tilde{R} = 1.19^{+0.10}_{-0.11}\,{\rm R}_\odot$.

If CVSO 30 is a binary, we might see it either nearly perpendicular to its orbital plane and/or it is a long periodic one, due to the fact that this object shows no line change in RV (van Eyken et al. 2012; Ciardi et al. 2015; Kounkel et al. 2019). We used high-resolution direct imaging data with adaptive optics of CVSO 30 from the European Southern Observatory (ESO) archive to estimate an upper limit on the possible separation, if CVSO 30 consists of two equally bright stars. The target was observed with Nasmyth Adaptive Optics System (NACO) at ESO's Very Large Telescope (VLT) on 2012 December 3 in jitter mode, using a jitter width of 4 arcsec, and the data were presented first in Schmidt et al. (2016). According to the ESO ambient conditions data base[4] the average Differential Image Moption Monitor (DIMM) seeing was 0.67 ± 0.03 arcsec and the average coherence time of the atmospheric fluctuations was 4.5 ± 0.2 ms during the *Ks*-band observations. The recorded data contain 15 cubes, each consisting of four images with an individual integration time of 15 s. The frames were flat-fielded with internal lamp flats, using the software package ESO ECLIPSE[5] (Devillard 1997). We show the reached detection limit for the *Ks*-band image of CVSO 30 in Fig. 7. The point spread function (PSF) of the star does not exhibit significant elongation in any direction, as illustrated in Fig. 8. It exhibits a FWHM of 6.4 ± 0.6 px. Adopting the pixel scale 13.265 ± 0.041 mas px^{-1} from Schmidt et al. (2016), this corresponds to 85 ± 8 mas. The diffraction limit of the 8.2 m VLT in the *Ks*-band is about 68 mas.

In order to test, at which separation an equally bright companion can be detected, we shifted the fully reduced image pixel by pixel, averaged it with the original frame and fit a two-dimensional Gaussian function with ESO-MIDAS (European Southern Observatory 2013). The artificial PSF becomes clearly elongated for equal bright sources with an angular separation larger 40 mas. This is in good agreement with Mugrauer & Ginski (2015), where they have detected a close binary companion of the exoplanet host star HD 142245 with NACO in the *Ks* band. That binary shows a clearly elongated PSF and an average separation of about 40 mas of its components.

Therefore, in our case a possible equal bright binary would have to be within a separation of 40 mas in order to have not been detected within the observations of CVSO 30. Based on this separation and a distance of 334^{+4}_{-3} pc (Bailer-Jones et al. 2021), we expect an upper limit of the orbital period of about 50 yr for the CVSO 30 system, assuming a total mass of 1 M$_\odot$ (corresponding to two times the mass given in Table 4). Additional observations are necessary to further constrain this upper limit, such as high-resolution follow-

[4] www.archive.eso.org/cms/eso-data/ambient-conditions.html
[5] https://www.eso.org/sci/software/eclipse/

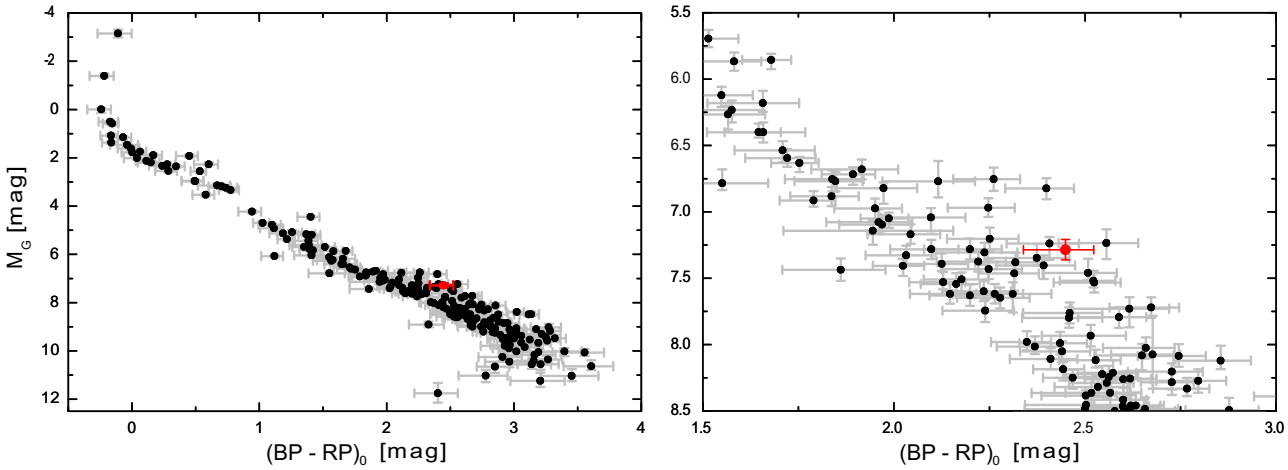

Figure 6. CMD of the 25 Ori cluster with CVSO 30 marked as red dot.

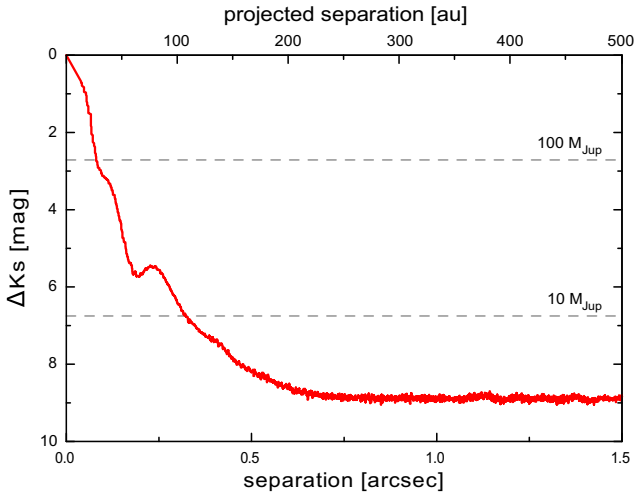

Figure 7. The reached detection limit (signal-to-noise ratio = 3) of the fully reduced NACO *K*s-band image of CVSO 30, which is presented in Fig. 8. The dashed horizontal lines show the expected *K*s-band magnitude differences for companions with 100 M_{Jup} and 10 M_{Jup} for an 8 Myr old system, according to models from Baraffe et al. (2015).

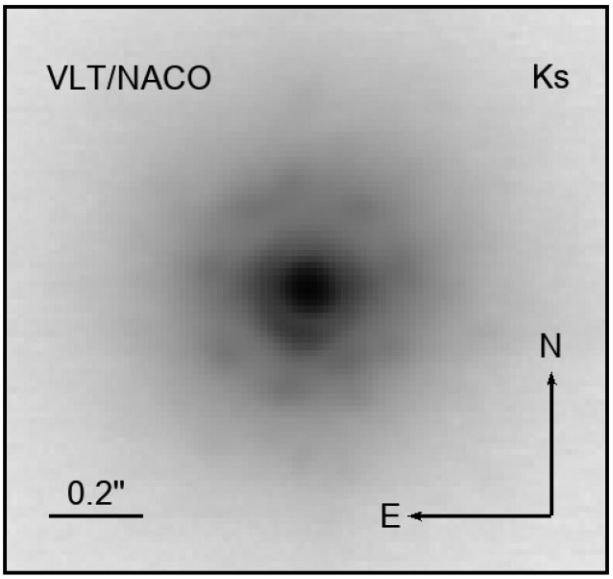

Figure 8. Direct imaging with adaptive optics of CVSO 30.

up spectroscopy or interferometric observations of CVSO 30 in the upcoming decades, as proposed by Koen (2020).

Otherwise, it might be also possible that CVSO 30 is redder (∼0.25 mag) than the typical cluster member. For a given mass, increasing metallicity shifts the stellar flux from the visual wavelengths range towards the infrared (Bonfils et al. 2005; Mann et al. 2015). Therefore, we searched for information regarding the metallicity of the 25 Ori members. The catalogue of Anders et al. (2019) contains 39 cluster stars, which are located in the CMD within CVSO 30's 3 σ uncertainties. These stars have a median metallicity of [Fe/H] = (0.40 ± 0.15) dex, which is consistent with CVSO 30 (see Table 4) within the standard deviation. Therefore, metallicity cannot explain the offset of CVSO 30 within the CMD. If CVSO 30 is actually redder than the other member stars, it needs an additional source, which contributes to the flux in the red wavelengths. This could be an orbiting co-rotating glowing cloud that shows significant Hα emission. We consider the possibility of this scenario in Section 6.

6 DISCUSSION AND CONCLUSION

In this article, we presented our follow-up photometric observations of the controversial discussed star CVSO 30, which was intensively monitored and analysed during the last decade, but still misses a clear explanation for its periodically dimming events. Our original YETI monitoring campaign of CVSO 30 started in 2010 (Raetz et al. 2016) and this is the continuation, which yields observations since fall 2014 that focused on the predicted time slots of the fading events.

We characterized CVSO 30 with data of the *Gaia* mission and catalogues. Our derived value of 1.69 ± 0.16 $R_\odot$ for its radius lies above those given in Briceño et al. (2005) (1.39 $R_\odot$) and Koen (2020) (1.41 $R_\odot$), but is consistent with them within 2 σ. In contrast, our radius does not fit the 0.45 ± 0.18 $R_\odot$ from Tanimoto et al. (2020).

The different dimming events, dip-A, dip-B, and dip-C, reported in Tanimoto et al. (2020) can be confirmed with our *R*-band observations. All three dips seem to have the same period but are phase shifted as illustrated in Fig. 1. Dip-A was detected by us in all nights if the observing window included the phase of −0.1 according to the ephemeris in equation (4), while dip-B, e.g. was not present

on 2017 January 5. Dip-A and dip-B were detected last in 2017 November and since then no more, as presented in the following light curves in Appendix A. That contradicts the detection of dip-B on 2018 November 9 by Tanimoto et al. (2020), because we have recorded the immediately following epoch without any fading event. Dip-A showed sometimes a 'v'-shaped profile and then in other epochs a 'u'-profile, as illustrated in Fig. 2. The same also applies to dip-B.

Dip-C was found first by Tanimoto et al. (2020) in autumn 2018. The first successful observation in our data set was in 2020 October. Five further detections followed until 2021 February. All light curves of dip-C yield 'u'-shape like minima.

For all three dips no clear trend was detectable in depth or duration, taking into account the entire period of the follow-up observations.

A circumstellar dust clump, consisting of an opaque core and a optically thin halo, cannot be excluded as cause for all dimming events based on their depths in the *R*- band and infrared. The existence of these clumps could be temporally limited and therefore explain the disappearance of dip-A and dip-B. As a result thereof, additional observations of dip-C in upcoming seasons are necessary to investigate whether this dip might vanish too.

However, such a theoretical clump would orbit around CVSO 30 at a distance of $(9.1 \pm 0.2) \times 10^{-3}$ au and have to face temperatures of 2268^{+161}_{-141} K. The expected condition at this location is above the sublimation temperatures for olivine, pyroxene, obsidian, iron, ice, and carbon, which were derived based on Kobayashi et al. (2011). Therefore, the clump will probably consist of gas rather than dust, which could be problematic for the interpretation by Grosson & Johns-Krull (2021). A gas cloud would fit better to a weak-line T Tauri star, because dust would have resulted into an infrared excess. Weak-line T Tauri stars have no or only an optically thin disc. Building on this consideration, the flux dips happen when the glowing cloud orbits behind the star (Jardine & van Ballegooijen 2005; Stauffer et al. 2017). A system with gas arranged in a circumstellar clumpy torus, could result from stellar winds at locations around the star where magnetic and gravitational forces are balanced (Collier Cameron & Robinson 1989; Jardine & van Ballegooijen 2005). In contrast, David et al. (2017) have presented a scenario, where a cloud, containing a minor amount of dust within the gas, around the young M 2.5 dwarf star RIK-210 could cause dimming up to ∼20 per cent. This star shows variable dimming events with a period of ∼5.7 d and the co-rotating orbit lies, as a result thereof, outside the sublimation distance. In the case of RIK-210 the dips would occur when the star is eclipsed by a dusty gas cloud.

Our case also involves co-rotating material, but we likely see secondary eclipses of light emitting gas. In this case, co-rotating plasma, which emits in a specific wavelength, causes the dimming events when it orbits behind the star and a reduced flux is measured (Palumbo et al. 2022). This orbiting plasma would also result in changes of the Hα emission line profile via RME when it moves in front of the star's disc as stated by Palumbo et al. (2022). This feature was not observed in the Hα measurements by Yu et al. (2015), who have recorded a set of spectra from CVSO 30 on 2013 December 12, which include the time of a photometric fading event. Their observations started/ended about 2 h before/after the minimum light and cover the timespan when the postulated glowing cloud would orbit behind the star. Therefore, a non-detection of the RME is well explainable with this scenario. Further Hα observations were presented by Johns-Krull et al. (2016). They have measured significant Hα excess emission within the spectra of CVSO 30 that changes its RV. The changing RV fits with the orbital period of the 'companion'. However, the measured RVs of the excess emission are often shifted in comparison to the predicted velocities (see fig. 9 in Johns-Krull et al. 2016) based on the ephemeris by van Eyken et al. (2012). Furthermore, the strength of the detected Hα excess is too large (about 70 per cent−80 per cent of the stellar equivalent width) to be caused by a single planet and needs an extended additional luminous volume, which surrounds it (Johns-Krull et al. 2016). All these observed features fit well with a co-rotating glowing cloud, which significantly emits flux in the optical *R*-band. David et al. (2017) stated that those clouds, consisting of partially ionized gas, can cause dimming events up to a few per cents when they move behind the star and the cloud's glowing could be the result of Paschen-continuum bound-free emission. The existence of partially ionized gas which emits in Hα is quite possible even at relatively low temperatures such as ∼2000 K (Rodríguez-Barrera et al. 2015).

Stauffer et al. (2017, 2018, 2021) had analysed a sample of photometric variable mid-to-late type M dwarfs in star-forming regions without signs of active accretion. These targets are rapidly rotating weak-line T Tauri stars with photometric periods shorter than 1 d. Subgroup of this sample are the 'stars with persistent flux dips', which additionally show two to four discrete flux dips in their phased light curve, with deepest depths of 2 per cent−7 per cent and durations ranging between 1 and 5 h. Their depths are largely stable but can suddenly disappear or become significantly weaker. Those changes in depth were observed after the detection of flare-like events. Similar fast rotating young M-dwarfs were found by Zhan et al. (2019). We detected some flare-like signals within our observations and they occurred after the last significant detection of dip-A and dip-B as illustrated in Fig. 1. Similar signatures can be found within the presented light curves in Figs 2 and 5 in van Eyken et al. (2012), which contain observations from 2009 December 26, 2010 January 1, 2010 January 7, and 2011 February 9. The scenario of Stauffer et al. (2017, 2018, 2021) has the flexibility to explain the disappearance and reappearance of the dimming events by changes in the geometry of the cloud without relying on active accretion. CVSO 30 shows the same characteristics in its light curve as the stars in Stauffer et al. (2017, 2018, 2021) and is also similar to the detected features in the light curve of TIC 234284556 (Palumbo et al. 2022). Therefore, the dimming events could originate from the currently not well-understood process of gas tori around young M dwarfs. Dip-A, dip-B, and dip-C seem to have the same orbital period, which is why their origin should have also the same distance to the star. This is a further indication for the theory of emitted light from magnetospheric clouds. Furthermore, the measured depth Δm in Table A1 would be the result of a secondary transit and consequently

$$\Delta m = -2.5 \log \left(\frac{F_\star}{F_\star + F_{\rm cloud}} \right), \tag{7}$$

where $F_\star$ represents the stellar flux and $F_{\rm cloud}$ the flux of the cloud. According to Stefan–Boltzmann law $F_\star \equiv R^2 \cdot T_{\rm eff}^4$ for the single star or $F_\star \equiv 2 \cdot \tilde{R}^2 \cdot T_{\rm eff}^4$ for the binary scenario, respectively.

We consider it well possible that flares due to reconnection of magnetic field lines and plasma tubes also lead to a reconfiguration of spots and groups of spots on the surface, which potentially affect the optical light curve. A strong X-ray flare in CVSO 30's light curve is reported in Czesla et al. (2019), where they have found no significant transit-induced variation within the expected time slot. That makes an orbiting planet even more questionable. The bell-like shape of the X-ray flare may also be owing to an accretion episode of CVSO 30. That fits with Yu et al. (2015), who came to the conclusion that CVSO 30 may be weakly accreting based on their measured strength and breadth of the Hα line profile.

Koen (2021) presents a model, where CVSO 30 is considered to be a binary and the variability is the result of stellar spots. From pure statistics the model can reproduce the detected variations inside

the *TESS* photometry, but the assumed filling factors e.g. $f \gtrsim 0.5$ for norm-2 models are very large and are based only on measurements in one filter. The detected fading events by *TESS* are dip-C according to Fig. 1, for which Tanimoto et al. (2020) had already ruled out the cool star-spot scenario based on their multiband photometry. The two different (apparent rotation) periods within the light curve of CVSO 30 (Bouma et al. 2020; Koen 2020) could also be caused by two spots of different latitudes, if the star (i.e. just one star) rotates differentially. Reinhold, Reiners & Basri (2013) and Reinhold & Gizon (2015) showed that the relative shear $\alpha = (P_{\rm max} - P_{\rm min})/P_{\rm max}$ increases with rotation period, by analysing thousands of stars from the *Kepler* mission (Koch et al. 2010). That fits with the two short-periodic signals of CVSO 30, which are close together in time.

To sum up the results of our monitoring campaign, we confirm the detection by Tanimoto et al. (2020) of three phase-shifted dimming events in the light curve of CVSO 30 with our photometric data between 2014 and 2021. Dip-A and dip-B were detected by us last in autumn 2017 and seem to have been vanished since then, while another dip-C was found after that, shifted in phase at about 180°. A Jovian planet as cause for the dimming events is unlikely, because of the colour effects of the transit depths and their disappearance within relatively short time-scales. We agree with Bouma et al. (2020) that orbiting clouds of gas at a Keplerian co-rotating radius are the most promising scenario to explain most changes in CVSO 30's light curve, because it does not need active accretion from a circumstellar disc and a changing shape of the dimming events can result from changes in the cloud's geometry. However, we consider that also stellar spots and at least some accretion seem to be going on CVSO 30. Nevertheless, further follow-up observations are necessary to find out if more flare-like events occur in the future, right before changes of dip-C can be detected. Furthermore, additional high-resolution spectroscopy and interferometric follow-up observations should be done to test CVSO 30's multiplicity status as proposed by Koen (2020).

ACKNOWLEDGEMENTS

This work is based on observations obtained with telescopes of the University Observatory Jena, operated by the Astrophysical Institute of the Friedrich-Schiller-Universität Jena. We thank B. Baghdasaryan, N. Belko, S. Buder, M. Dadalauri, M. Geymeier, H. Gilbert, A. Gonzalez, F. Hildebrandt, H. Keppler, O. Lux, S. Masda, P. Protte, J. Trautmann, A. Trepanowski, and S. Schlagenhauf, who have been involved in some observations of this project, obtained at the University Observatory Jena.

This research was partly based on data obtained at the 1.5 m telescope of the Sierra Nevada Observatory (Spain), which is operated by the Consejo Superior de Investigaciones Científicas (CSIC) through the Instituto de Astrofísica de Andalucía. We thank J.F. Aceituno and V. Casanova for their help with the observations.

This publication is partly based on observations made with ESO Telescopes at the La Silla Paranal Observatory under programme ID 090.C-0448(A).

RB, RN, and MM acknowledge the support of the DFG priority programme SPP 1992 'Exploring the Diversity of Extrasolar Planets' in projects NE 515/58-1 and MU 2695/27-1.

We acknowledge financial support from the Spanish Agencia Estatal de Investigación of the Ministerio de Ciencia, Innovación y Universidades and the ERDF through projects PID2019-109522GB-C52 and AYA2016-79425-C3-3-P, and the Centre of Excellence 'Severo Ochoa' award to the Instituto de Astrofísica de Andalucía (SEV-2017-0709).

We thank R. Errmann for developing and providing the photometry routine 'AUTOMAT.PY' and also C. Broeg for his program 'PHOTOMETRY'.

This publication makes use of data products of the SIMBAD and VizieR data bases, operated at CDS, Strasbourg, France. We also thank the *Gaia* Data Processing and Analysis Consortium of the ESA for processing and providing the data of the *Gaia* mission. We thank the MAST portal for providing the *TESS* photometric results and the MESA Isochrones & Stellar Tracks website for the bolometric correction tables.

We thank the referee for helpful comments, which improved our manuscript.

DATA AVAILABILITY

The data underlying this article are available in this manuscript. The detrended (if applicable) and also the original photometric measurements of all light curves are provided as online supplementary material.

REFERENCES

Anders F. et al., 2019, A&A, 628, A94
Bailer-Jones C. A. L., Rybizki J., Fouesneau M., Demleitner M., Andrae R., 2021, AJ, 161, 147
Baraffe I., Homeier D., Allard F., Chabrier G., 2015, A&A, 577, A42
Barnes J. W., van Eyken J. C., Jackson B. K., Ciardi D. R., Fortney J. J., 2013, ApJ, 774, 53
Bertin E., Arnouts S., 1996, A&AS, 117, 393
Bonfils X., Delfosse X., Udry S., Santos N. C., Forveille T., Ségransan D., 2005, A&A, 442, 635
Bouma L. G. et al., 2020, AJ, 160, 86
Brát L., Poddaný S., Pejcha O., Zejda M., 2010, in Prša A., Zejda M., eds, ASP Conf. Ser. Vol. 435, Binaries - Key to Comprehension of the Universe. Astron. Soc. Pac., San Francisco, p. 443
Briceño C., Calvet N., Hernández J., Vivas A. K., Hartmann L., Downes J. J., Berlind P., 2005, AJ, 129, 907
Broeg C., Fernández M., Neuhäuser R., 2005, Astron. Nachr., 326, 134
Cardelli J. A., Clayton G. C., Mathis J. S., 1989, ApJ, 345, 245
Choi J., et al., 2016, ApJ, 823, 102
Ciardi D. R. et al., 2015, ApJ, 809, 42
Claret A., Bloemen S., 2011, A&A, 529, A75
Collier Cameron A., Robinson R. D., 1989, MNRAS, 236, 57
Czesla S., Schneider P. C., Salz M., Klocová T., Schmidt T. O. B., Schmitt J. H. M. M., 2019, A&A, 629, A5
David T. J. et al., 2017, ApJ, 835, 168
Devillard N., 1997, The Messenger, 87, 19
Eastman J., Siverd R., Gaudi B. S., 2010, PASP, 122, 935
Errmann R. et al., 2014, Astron. Nachr., 335, 345
Errmann R., 2016, PhD thesis, Univ. Jena
European Southern Observatory, 2013, Astrophysics Source Code Library, record ascl:1302.017
Gaia Collaboration, 2021, A&A, 649, A1
Green G. M., Schlafly E., Zucker C., Speagle J. S., Finkbeiner D., 2019, ApJ, 887, 93
Grosson T. A., Johns-Krull C. M., 2021, Res. Notes Am. Astron. Soc., 5, 264
Huang P. C. et al., 2019, ApJ, 871, 183
Jardine M., van Ballegooijen A. A., 2005, MNRAS, 361, 1173
Johns-Krull C. M. et al., 2016, ApJ, 830, 15
Kobayashi H., Kimura H., Watanabe S. i., Yamamoto T., Müller S., 2011, Earth, Planets and Space, 63, 1067
Koch D. G. et al., 2010, ApJ, 713, L79
Koen C., 2015, MNRAS, 450, 3991
Koen C., 2020, MNRAS, 494, 4349
Koen C., 2021, A&A, 647, L1
Kounkel M. et al., 2018, AJ, 156, 84

Kounkel M. et al., 2019, AJ, 157, 196
Mann A. W., Feiden G. A., Gaidos E., Boyajian T., von Braun K., 2015, ApJ, 804, 64
Mugrauer M., Berthold T., 2010, Astron. Nachr., 331, 449
Mugrauer M., Ginski C., 2015, MNRAS, 450, 3127
Neuhäuser R. et al., 2011, Astron. Nachr., 332, 547
Neuhauser R., Torres G., Frink S., Covino E., Alcala J. M., 1997, Mem. Soc. Astron. Italiana, 68, 1061
Onitsuka M., Fukui A., Narita N., Hirano T., Kusakabe N., Ryu T., Tamura M., 2017, PASJ, 69, L2
Ortiz J. L., Gutiérrez P. J., Santos-Sanz P., Casanova V., Sota A., 2006, A&A, 447, 1131
Palumbo E. K., Montet B. T., Feinstein A. D., Bouma L. G., Hartman J. D., Hillenbrand L. A., Gully-Santiago M. A., Banks K. A., 2022, ApJ, 925, 75
Poddaný S., Brát L., Pejcha O., 2010, New Astron., 15, 297
Prša A. et al., 2016, AJ, 152, 41
Queiroz A. B. A. et al., 2020, A&A, 638, A76
Raetz S. et al., 2016, MNRAS, 460, 2834
Reinhold T., Gizon L., 2015, A&A, 583, A65
Reinhold T., Reiners A., Basri G., 2013, A&A, 560, A4
Ricker G. R. et al., 2015, J. Astron. Telesc. Instrum. Syst., 1, 014003
Rodríguez-Barrera M. I., Helling C., Stark C. R., Rice A. M., 2015, MNRAS, 454, 3977
Schmidt T. O. B. et al., 2016, A&A, 593, A75
Siwak M., Dróżdż M., Gut K., Winiarski M., Ogłoza W., Stachowski G., 2019, Acta Astron., 69, 227
Stauffer J. et al., 2017, AJ, 153, 152
Stauffer J. et al., 2018, AJ, 155, 63
Stauffer J. et al., 2021, AJ, 161, 60
Tanimoto Y. et al., 2020, PASJ, 72, 23
Tody D., 1993, in Hanisch R. J., Brissenden R. J. V., Barnes J., eds, ASP Conf. Ser. Vol. 52, Astronomical Data Analysis Software and Systems II. Astron. Soc. Pac., San Francisco, p. 173
Unsöld A., Baschek B., 2005, Der neue Kosmos. Einführung in die Astronomie und Astrophysik, 7th edn, Springer-Verlag, Berlin
van Eyken J. C. et al., 2012, ApJ, 755, 42
Wang S., Chen X., 2019, ApJ, 877, 116
Yu L. et al., 2015, ApJ, 812, 48
Zhan Z. et al., 2019, ApJ, 876, 127

SUPPORTING INFORMATION

Supplementary data are available at *MNRAS* online.

Supplementary_Data.tar.gz

Please note: Oxford University Press is not responsible for the content or functionality of any supporting materials supplied by the authors. Any queries (other than missing material) should be directed to the corresponding author for the article.

APPENDIX A: LIGHT CURVES AND RESULTS OF THE TRANSIT FITTING

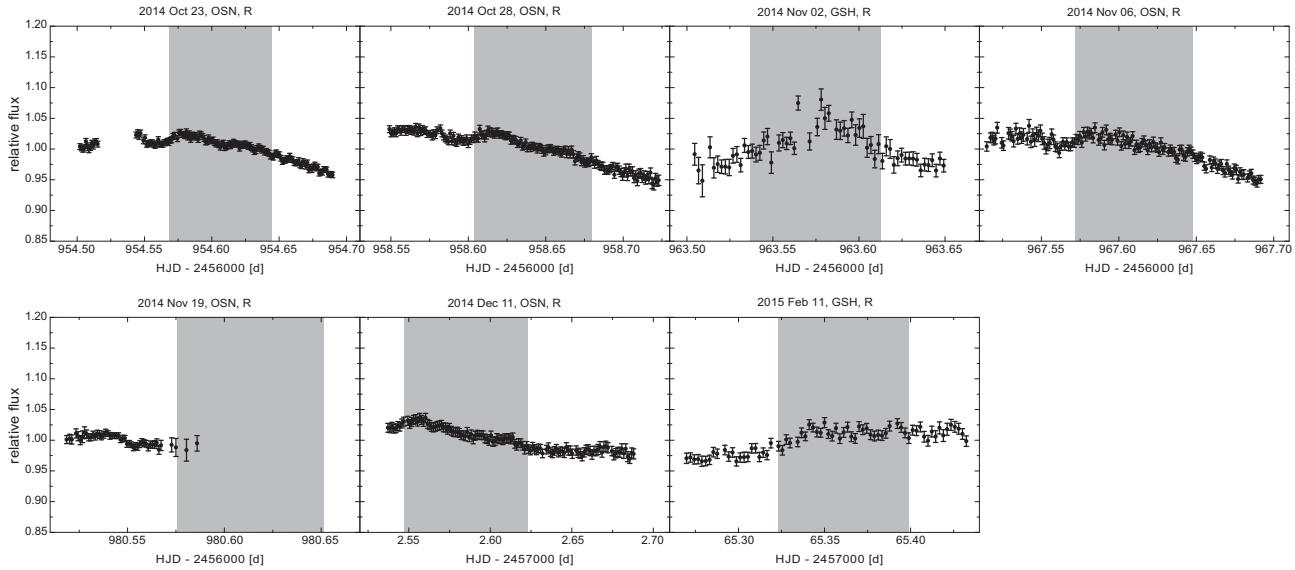

Figure A1. All recorded light curves of CVSO 30 in season 2014/2015. The grey shaded areas show the time slots of the expected fading events, fixed at period and mid-time from Tanimoto et al. (2020). The value for the duration was taken from van Eyken et al. (2012) and is fixed in all light curves.

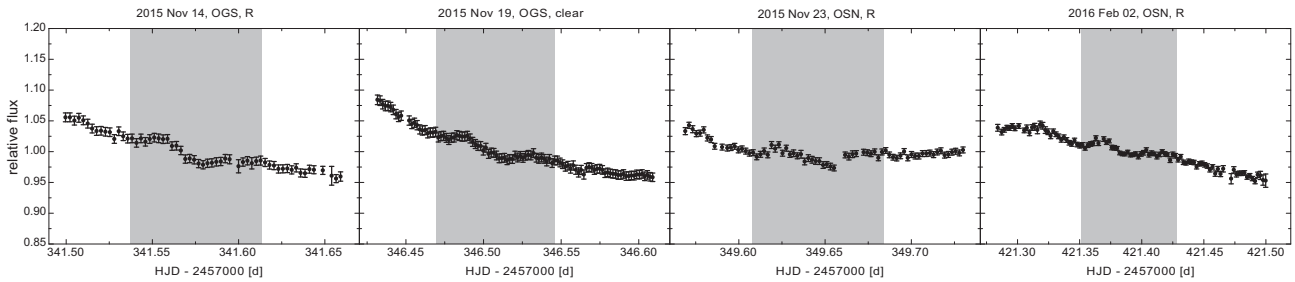

Figure A2. Same as Fig. A1 but for season 2015/2016.

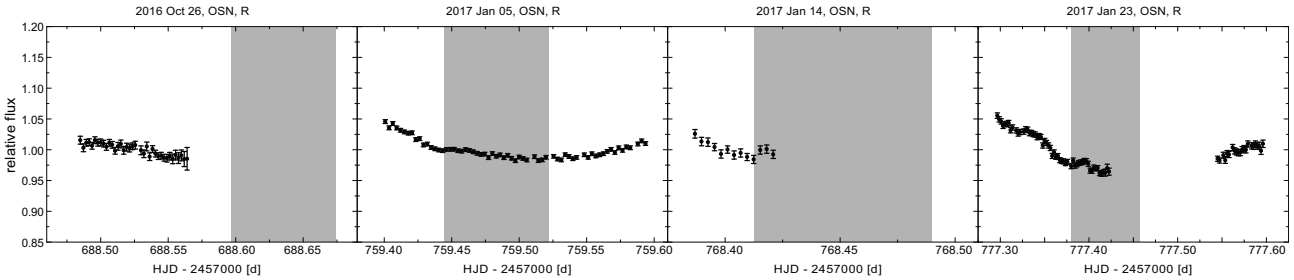

Figure A3. Same as Fig. A1 but for season 2016/2017.

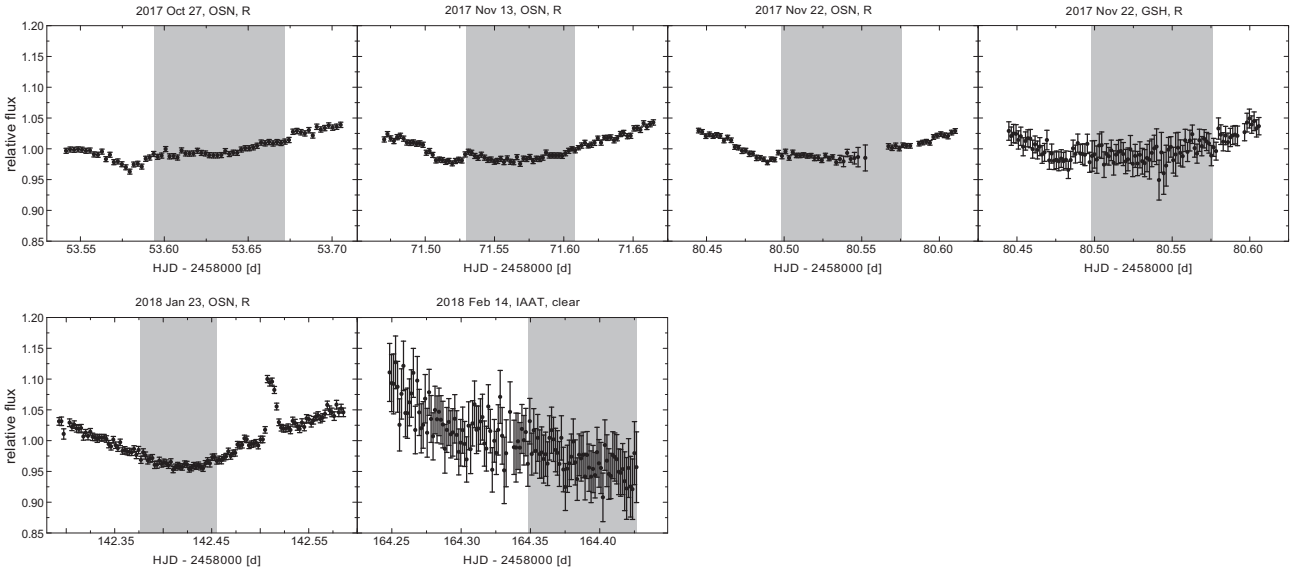

Figure A4. Same as Fig. A1 but for season 2017/2018.

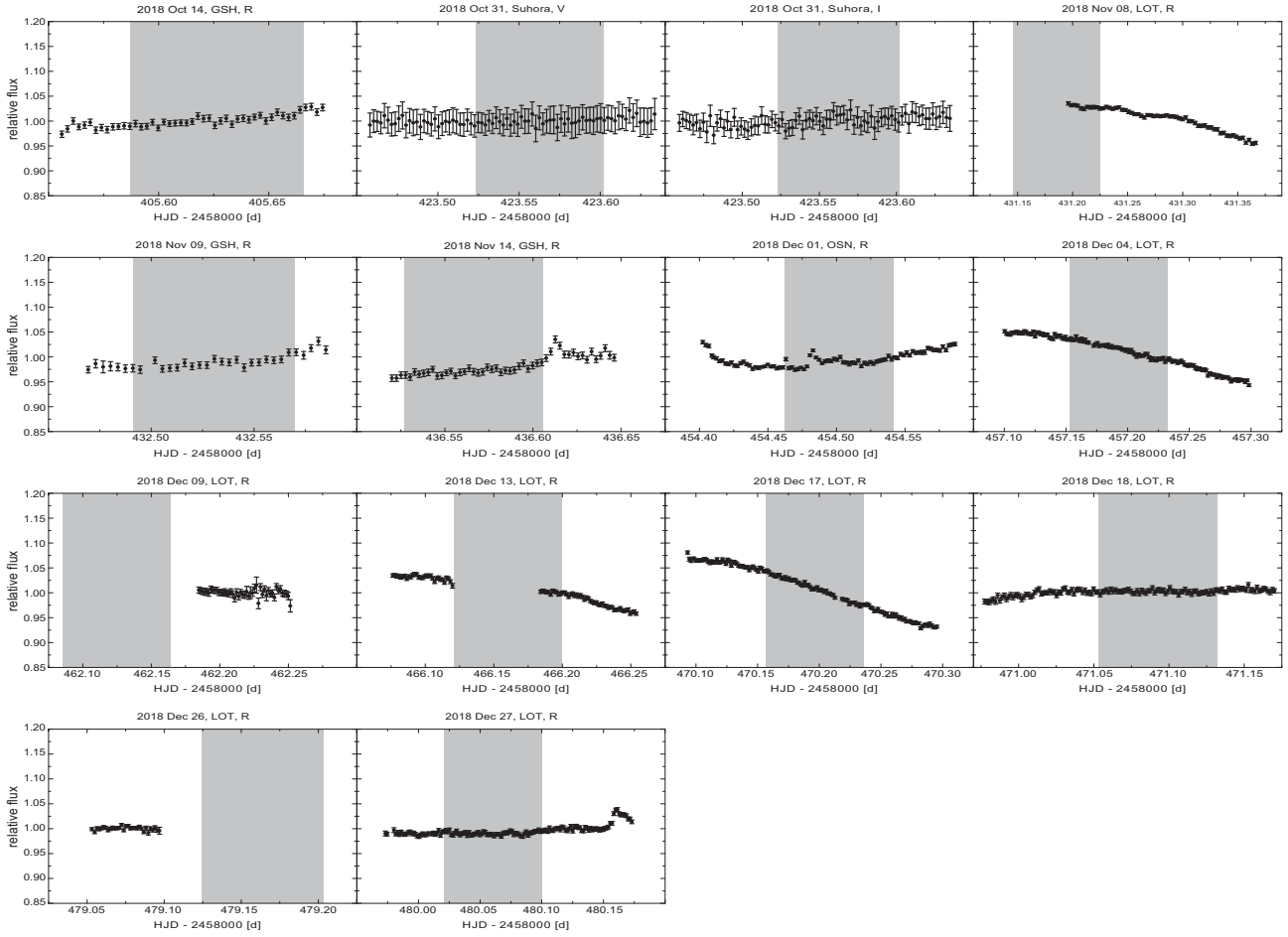

Figure A5. Same as Fig. A1 but for season 2018/2019.

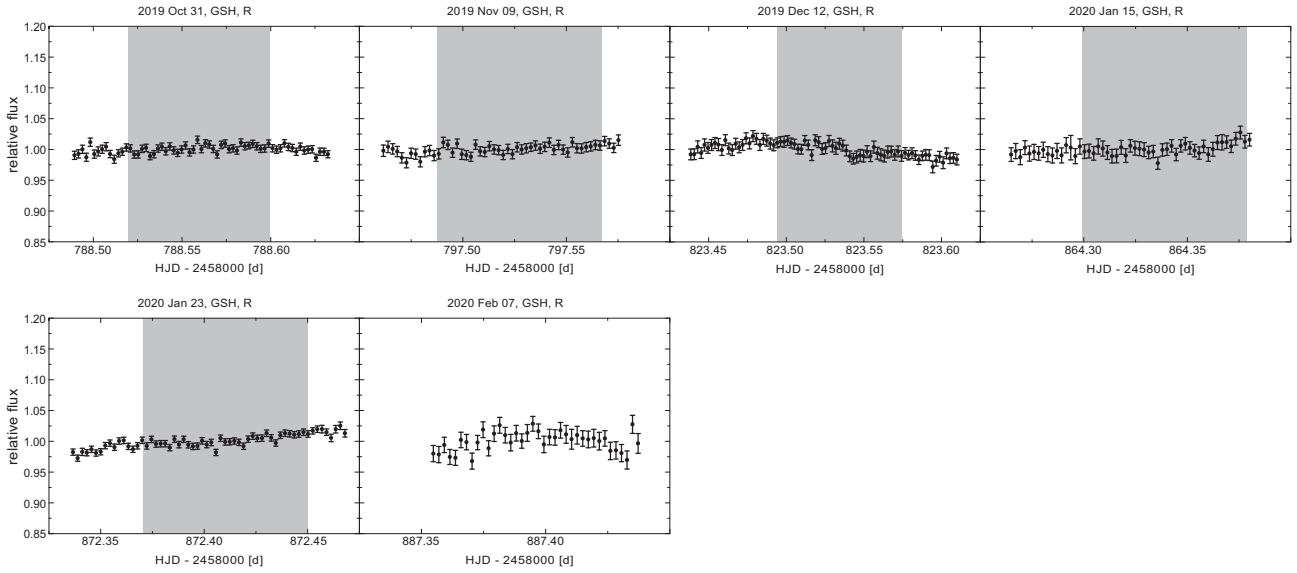

Figure A6. Same as Fig. A1 but for season 2019/2020.

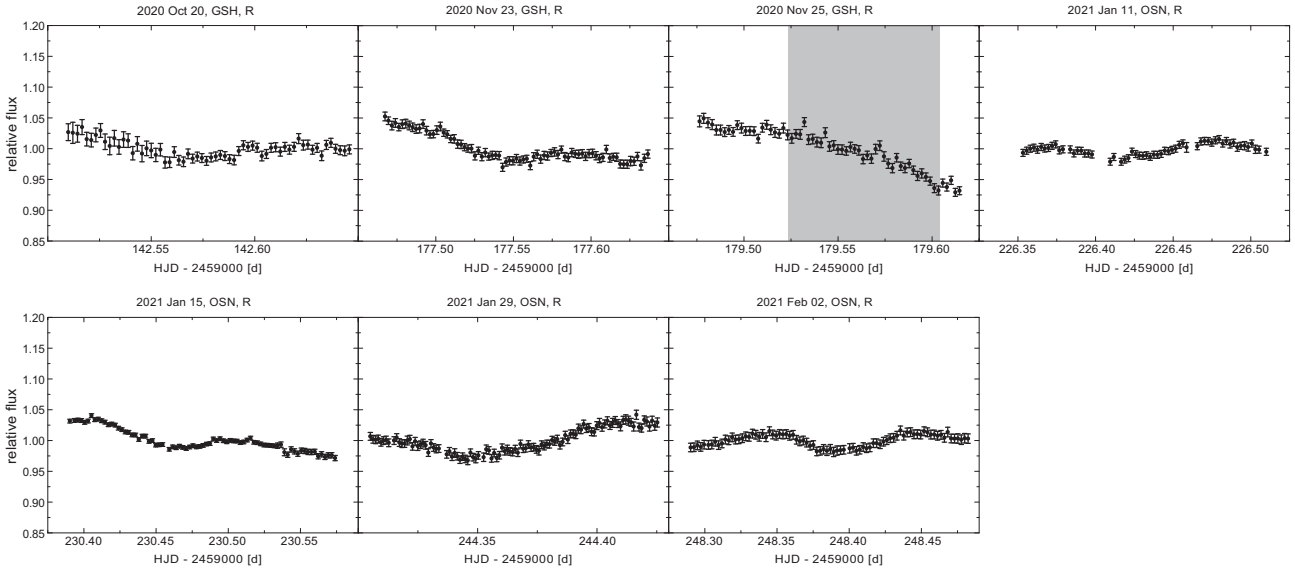

Figure A7. Same as Fig. A1 but for season 2020/2021.

Table A1. Results of the transit fitting for the 29 significant detected fading events of CVSO 30 carried out with ETD. We list for each epoch the date (start of observation), transit centre time (T_c), duration (T_{14}), depth (Δm), and orbit phase according to the ephemeris from Tanimoto et al. (2020).

Epoch	Date	T_c (BJD_{TDB})	T_{14} (min)	Δm (mmag)	Orbit phase
Dip-A					
3146	2014 Oct 23	2456954.5611 ± 0.0007	43.6 ± 4.8	16.5 ± 1.7	−0.103 ± 0.006
3155	2014 Oct 28	2456958.5946 ± 0.0011	64.7 ± 6.3	18.5 ± 2.0	−0.107 ± 0.007
3175	2014 Nov 06	2456967.5630 ± 0.0011	53.3 ± 7.1	22.5 ± 2.8	−0.107 ± 0.007
3393	2015 Feb 11	2457065.3098 ± 0.0021	113.4 ± 14.6	29.1 ± 4.6	−0.116 ± 0.008
4009	2015 Nov 14	2457341.5318 ± 0.0015	77.6 ± 10.2	14.0 ± 2.0	−0.098 ± 0.008
4020	2015 Nov 19[a]	2457346.4643 ± 0.0009	87.1 ± 6.1	17.8 ± 1.8	−0.098 ± 0.007
4027	2015 Nov 23	2457349.6013 ± 0.0014	82.0 ± 9.3	18.2 ± 2.4	−0.102 ± 0.008
4187	2016 Feb 02	2457421.3482 ± 0.0012	70.8 ± 7.8	17.1 ± 1.7	−0.095 ± 0.008
4941	2017 Jan 05	2457759.4385 ± 0.0012	55.4 ± 7.2	11.3 ± 1.4	−0.101 ± 0.008
4981	2017 Jan 23	2457777.3770 ± 0.0011	89.4 ± 7.3	24.7 ± 1.7	−0.096 ± 0.008
5597	2017 Oct 27	2458053.5797 ± 0.0008	44.9 ± 5.2	22.1 ± 2.4	−0.121 ± 0.009
5637	2017 Nov 13	2458071.5155 ± 0.0008	54.3 ± 5.1	22.1 ± 2.0	−0.121 ± 0.009
5657	2017 Nov 22[b]	2458080.4855 ± 0.0009	60.9 ± 5.9	17.5 ± 1.7	−0.117 ± 0.009
5657	2017 Nov 22[c]	2458080.4781 ± 0.0016	35.0 ± 10.0	20.7 ± 5.4	−0.133 ± 0.009
Dip-B					
3146	2014 Oct 23	2456954.6072 ± 0.0013	37.6 ± 7.6	7.9 ± 1.5	0.000 ± 0.007
3155	2014 Oct 28	2456958.6410 ± 0.0015	52.5 ± 8.8	9.0 ± 1.5	−0.004 ± 0.007
3253	2014 Dec 11	2457002.5839 ± 0.0015	38.2 ± 8.6	7.1 ± 1.5	−0.005 ± 0.007
4009	2015 Nov 14	2457341.5786 ± 0.0007	57.2 ± 4.6	25.2 ± 1.9	0.006 ± 0.007
4020	2015 Nov 19[a]	2457346.5101 ± 0.0007	58.9 ± 6.1	16.7 ± 1.2	0.004 ± 0.007
4027	2015 Nov 23	2457349.6486 ± 0.0010	62.4 ± 5.7	20.9 ± 1.8	0.004 ± 0.007
4187	2016 Feb 02	2457421.3892 ± 0.0012	55.5 ± 7.1	14.8 ± 1.7	−0.004 ± 0.008
5597	2017 Oct 27	2458053.6392 ± 0.0021	57.5 ± 12.7	7.7 ± 1.6	0.012 ± 0.010
5637	2017 Nov 13	2458071.5703 ± 0.0025	122.1 ± 11.0	8.9 ± 1.1	0.001 ± 0.010
Dip-C					
8026	2020 Oct 20	2459142.5694 ± 0.0024	92.7 ± 14.5	17.2 ± 2.6	−0.505 ± 0.013
8104	2020 Nov 23	2459177.5427 ± 0.0012	119.2 ± 7.0	30.0 ± 1.7	−0.509 ± 0.012
8213	2021 Jan 11	2459226.4220 ± 0.0009	148.7 ± 4.5	33.4 ± 1.2	−0.501 ± 0.012
8222	2021 Jan 15	2459230.4588 ± 0.0007	138.9 ± 4.0	33.5 ± 1.0	−0.498 ± 0.012
8253	2021 Jan 29	2459244.3623 ± 0.0010	129.4 ± 5.4	30.4 ± 1.4	−0.491 ± 0.012
8262	2021 Feb 02	2459248.3965 ± 0.0006	134.9 ± 3.3	37.2 ± 0.9	−0.494 ± 0.012

Note. [a]Clear filter. [b]OSN. [c]GSH.

This paper has been typeset from a Microsoft Word file prepared by the author.